



Original Research Paper

# Application of computationally inexpensive CFD model in steady-state and transient simulations of pulverized sewage sludge combustion



Benjamin Ortner<sup>a</sup>, Christian Schmidberger<sup>b</sup>, Hannes Gerhardt<sup>a</sup>, René Prieler<sup>a</sup>, Hartmuth Schröttner<sup>c</sup>, Christoph Hochenauer<sup>a</sup>

<sup>a</sup>Institute of Thermal Engineering, Faculty of Mechanical Engineering and Economic Sciences, Graz University of Technology, Inffeldgasse 25B, 8010 Graz, Austria

<sup>b</sup>Institute of Combustion and Power Plant Technology, Faculty 4 - Energy-, Process- and Bio-Engineering, University of Stuttgart, Pfaffenwaldring 23, 70569 Stuttgart, Germany

<sup>c</sup>Austrian Centre for Electron Microscopy and Nanoanalysis, Steyrergasse 17, 8010 Graz, Austria

## ARTICLE INFO

### Article history:

Received 20 March 2023

Received in revised form 17 August 2023

Accepted 18 October 2023

Available online 9 November 2023

### Keywords:

Sewage sludge combustion

Flamelet modelling

Entrained flow furnace

Slag deposition

## ABSTRACT

The combustion process of pulverized fuels with high ash contents, such as sewage sludge, is significantly impacted by the amount of slag deposition in a furnace. A CFD model based on the Steady Diffusion Flamelet (SFM) approach was applied to numerically simulate the combustion of pulverized sewage sludge in a drop tube furnace. Steady-state solutions of the Reynolds-Averaged Navier–Stokes (RANS) equations already displayed good agreement with species and temperature measurements. Still, they failed to accurately predict the significant amount of ash trapped on the internal furnace surfaces (minimum deposition of 28% of the generated ash versus 5% predicted by the RANS simulations). The SFM-based CFD model's computational efficiency enabled the conduction of large eddy simulations (LES), significantly improving the model's predictive capabilities (27% of the generated ash deposited). Additionally, the transient simulations further improved the agreement with temperature measurement data. A novel initialization procedure was developed, which allowed the transient LES simulations to be conducted in a computationally efficient manner. The SFM-based model can effectively support research and development efforts, even for large-scale systems which require high cell counts. It provides valuable insights during the early design phases of industrial furnaces for pulverized sewage sludge combustion.

© 2023 The Society of Powder Technology Japan. Published by Elsevier B.V. and The Society of Powder Technology Japan. This is an open access article under the CC BY license (<http://creativecommons.org/licenses/by/4.0/>).

## 1. Introduction

As worldwide hygiene standards are rising, especially in emerging markets and developing countries, where the population is also growing, higher amounts of municipal waste are expected to be generated in the near future. Consequently, more wastewater treatment residues in the form of sewage sludge will occur. The application of sewage sludge in agriculture is increasingly avoided since it is not only composed of organic materials with fertilizing properties. It also contains materials such as heavy metals, as reported by Udayanga et al. [1] and pharmaceutical residues [2], which can be harmful to aquatic and terrestrial ecosystems. Another way of sewage sludge utilization is the co-incineration with pulverized coal. This has been studied by researchers such as Namkung et al. [3], including the effects of ash agglomerations. It is also frequently co-combusted with municipal waste, as reported by Roy et al. [4]. Alternative ways to exploit the remaining energy content in sewage sludge, such as gasification, are a subject

of increasing interest in the European Union, as reported by Bianchini et al. [5]. A recent review was published by Quan and Kamyab et al. [6], regarding the application of gasification and combustion in sewage sludge treatment.

In addition to the thermal exploitation of the energy content in sewage sludge, the resulting ash offers valuable ingredients such as phosphorus. As pointed out by Atienza-Martinez, these can be recovered in the sense of a circular economy [7]. Especially in Europe, which is heavily dependent on the importation of phosphorus, a sustainable concept like this seems very promising. The underlying processes are often highly energy-intensive. Therefore, a logical initial step involves implementing a conversion process that effectively harnesses the energy content present in dried and ground (pulverized) sewage sludge (PSS). In one concept, the PSS, ground to small particle sizes, is mono-combusted in a furnace with high turbulence. During this process, the ash undergoes melting, resulting in the formation of slag that is subsequently collected. Computational fluid dynamics (CFD) simulations are a widespread and popular tool for research and development of industrial furnaces, also regarding combustion and agglomeration modelling. We aim

E-mail address: [benjamin.ortner@tugraz.at](mailto:benjamin.ortner@tugraz.at) (B. Ortner)

**Nomenclature**

*Abbreviations*

ar	as received
CEQ	Chemical equilibrium model
CFD	Computational fluid dynamics
DIA	Dynamic image analysis
DPM	Discrete phase model
DRW	Discrete random walk
EAR	Excess air ratio
EDC	Eddy dissipation concept
EDM	Eddy dissipation model
LCV	Lower calorific value
LES	Large eddy simulation
MFC	Mass flow controller
ppm	Parts per million
PSD	Particle size distribution
PSS	Pulverized sewage sludge
RANS	Reynolds-averaged Navier-Stokes
RRSB	Rosin-Rammler-Sperling-Bennett (PSD)
RSM	Reynolds stress model
SEM	Scanning electron microscopy
SFM	Steady diffusion Flamelet
SGS	Sub-grid scale
TC	Thermocouple
TGA	Thermogravimetric analysis
UDF	User-defined function
WALE	Wall adapting local eddy-viscosity
WSGGM	Weighted sum of gray gases model

*Greek symbols*

$\rho$	Density
--------	---------

$\varepsilon$	Emissivity
$\sigma$	Boltzmann constant
$\lambda$	Thermal conductivity
$\psi$	Sphericity (Wadell)
$\mu, \mu_t$	Dynamic viscosity, turbulent viscosity
$\Theta_r$	Radiation temperature
$\Omega_r$	Solid angle
$\bar{\chi}_{st}$	Scalar dissipation

*Roman symbols*

$A$	Area
$Bi$	Biot number
$c_p$	Specific heat (constant pressure)
$d$	Diameter
$\bar{f}$	Mean mixture fraction
$f'^2$	Mixture fraction variance
$g$	Gravity
$G$	Incident radiation
$h$	Heat transfer coefficient
$I$	Radiation intensity
$k$	Turbulence kinetic energy
$m$	Mass
$Nu$	Nusselt number
$Pr$	Prandtl number
$Re$	Reynolds number
$S$	Strain rate
$t$	Time
$T$	Temperature
$u, v, w$	Velocity components
$V$	Volume

to apply CFD to the PSS conversion process with a computationally inexpensive model as described in this paper.

1.1. Combustion, gasification and ash agglomeration modelling of pulverized sewage sludge

Wang et al. [8] noted that the combustion of PSS can be closely compared to pulverized coal combustion since both contain considerable amounts of water content, volatile matter, fixed carbon and ash. The lower heating value (on a dry basis) of around 12 MJ/kg [9] of PSS is, of course, smaller due to the high amount of ash. On a wet basis, with water contents beyond 60% (wet sludge), this value can be negative [10]. In this case, only co-

combustion is an option. Therefore we focus on pre-dried and ground sludge in this study.

For overview purposes, Table 1 states often encountered water content-, volatile release-, fixed carbon- and ash mass fractions in PSS, and their relation to lignite. From this perspective, PSS can be classified as a very volatile-rich and high-ash content fuel. This relates mainly to the organic content of the material, which is most relevant for the combustion modelling. The ash fraction sums up all remaining contents after combustion, including e.g., silica and iron-oxides but also phosphates. Therefore, the ash is the basis for further processing [7], such as phosphorus recovery.

Due to the fact that more than 90% of the ash-free components are released as volatiles, Werther et al. [11] describe the combustion characteristics of sewage sludge in a fluidized bed as dominated by gas-phase reactions. They even describe the combustion characteristics of sewage sludge as close to that of gaseous fuels [12]. Cui et al. noted that the dehydration and devolatilization of particles can take place simultaneously [13]. This overlap becomes more pronounced when particle heating rates are very high. Therefore, volatiles emitted from PSS particles at high heating rates can be, by approximation, considered to be a reasonably homogeneous, multi-species mixture of water vapor, carbon oxides and short- and long-chained hydrocarbons (tars). Researchers have used species transport models such as the eddy dissipation model [14,15] or highly detailed chemistry involving eddy dissipation concept models [16,17] while applying a surrogate approach. Based on the aforementioned properties of PSS combustion, we developed a Flamelet-based surrogate combustion model for PSS in our previous study [18].

**Table 1**

Order of magnitude for PSS particle properties in proximate analysis and comparison to lignite.

Property from proximate analysis	Mass fraction common for PSS	Comparison to lignite
Water content	< 20%	generally higher for PSS, low in our case because of effective pre-drying
Volatile release	> 40%	generally higher for PSS, much higher in our case
Fixed carbon	< 4%	generally lower for PSS, much lower in our case
Ash (slag)	> 40%	generally higher for PSS, very high in our case

Besides reaction chemistry, which influences the spatial distributions of temperatures and species concentrations inside a furnace, it is of important interest to know the amount of slag that is inevitably accrued at the furnace walls. This is especially true when high-ash fuels such as PSS are considered. After slag droplets are trapped at the furnace walls, they may flow downward, driven by gravity and cause a significant slag flow. Chen et al. [19] published a CFD simulation of slagging in a vertically oriented oxy-coal combustor, which is quite similar to the one in our study. However, a reliable prediction of slag accretions requires a reasonable prediction of contacts between ash particles and walls. Regarding turbulence modelling, Knoll et al. [20] noted that the application of transient large eddy simulations (LES) helped to improve particle-wall contact predictions significantly, compared to commonly used steady-state models, which model turbulence based on eddy viscosity approaches. These researchers considered inert particles inside a similar vertical furnace. LES with reactive particles have been performed by Watanabe et al. [21,22] in pulverized coal combustion while applying a multiple-mixture-fraction Flamelet model for their chemistry considerations. Wen et al. have shown that their Flamelet model can outperform the eddy break-up model [23] and expanded their approach further using multi-regime Flamelet models to account for partially premixed regions as well as for different particle sizes [24,25]. Rieth et al. presented Flamelet-based LES simulations of a semi-industrial pulverized coal furnace [26], also in a highly resolved domain [27]. Watanabe et al. presented a highly detailed LES coal gasification model in an entrained flow gasifier, including slag flow, using a model with an also very high cell count of 120 million [28] in a perspective article. Akaotsu et al. applied a Flamelet/progress-variable approach to LES of pulverized coal [29]. Evidently, there is a significant amount of literature about Flamelet- and LES modelling of pulverized coal, but to our knowledge, no comparable simulation models for PSS combustion have been published.

### 1.2. Objective of this paper

This study aims to apply a computationally inexpensive, Flamelet-based combustion model in transient LES simulations. Thereby, the significant prediction inaccuracy of conventional steady-state RANS methods can be overcome. The modelling approach described in this paper involves a novel initialization procedure, which further helps to reduce the necessary simulation times to obtain statistically steady results. These results are compared to experimental data from semi-industrial trials.

## 2. Experimental furnace operation

This section provides an overview of the fuel material and the furnace on which the experiments were conducted.

### 2.1. PSS material properties

An elementary and proximate analysis result of the investigated PSS is provided in Table 2. The water content after drying lies at 10%. The dry and ash-free matter has a high carbon content of 0.508, but considerable amounts of nitrogen and sulfur are also present. High ash- and volatile contents were determined, as is typical for sewage sludge. In contrast, the fixed carbon fraction is low, indicating the dominance of volatile combustion. In comparison, lignite can reach fixed carbon values of 40 to 50% as studies by Al-abbas [30] and Steibel [31] have shown, and heterogeneous surface reactions are much more relevant.

**Table 2**

Elementary and proximate analysis of the considered PSS, daf = dry, ash-free.

Elementary analysis	Mass fraction	Proximate analysis	Mass fraction
daf			
C	0.508	Water content	0.100
H	0.068	Volatile matter	0.409
O	0.341	Fixed carbon	0.041
N	0.064	Ash	0.450
S	0.019		

Since individual particles will be tracked during the simulations and drag and heat transfer are sensitive to particle sizes and shapes, we included a dynamic image analysis (DIA) of the material in this study. The results are summarized in Fig. 1. The highly accurate particle size distribution (PSD) measurement is given in Fig. 1a, in which mass fractions in certain size bands are indicated with crosses. The vast majority of particles are of a size smaller than 100  $\mu\text{m}$ . Further, the PSD seems to be bimodal and quite wide. Outliers can reach 1.6 mm in length. Moreover, the DIA provides shape information based on actual particle imaging, which is provided in Fig. 1b. We use the sphericity as a shape parameter in this study. According to Wadell, it is defined as  $\psi = s/S$ , wherein  $s$  is the surface area of a sphere with the same volume as the particle, and  $S$  is the actual surface area of the particle [32]. The overwhelming majority of particles exhibit sphericities in the range of 0.8 to 0.9. This is further confirmed by additional scanning electron microscope (SEM) images as shown in Fig. 1c, showing some large and some fine particles and their rough surface. An image of fiber-like particles in the PSD is offered in Fig. 1d. The outliers in the PSD are attributed to these longer fibers. The falling sphericity values at larger particle sizes support this conclusion.

Thermogravimetric Analyzer (TGA) measurements in  $\text{N}_2$  revealed that the PSS displayed a gradual mass loss over a wide temperature range, as shown in Fig. 2a. The effect starts even below 100  $^\circ\text{C}$ , indicating the water content's drying and initiating evaporation. A significant stage was observed between 200 and 300  $^\circ\text{C}$ . After that, a gradual mass loss occurs until all volatile components are released. Fig. 2b shows a *FactSage*-calculated, temperature-dependent specific heat curve for the PSS ash. The specific heat required to heat up the material gradually increases with temperature. The melting enthalpy effect appears as peaks in the  $c_p$  curve. In the same way, it is also implemented in the CFD simulation. Another important measured property is the particle density, which was determined as 1,840  $\text{kg}/\text{m}^3$  using a helium pycnometer. The particle's thermal conductivity was estimated to a constant value of 1.0  $\text{W}/(\text{m} \cdot \text{K})$ , which is a reasonable value for ash particles [33]. The described material properties were used in the CFD simulations.

### 2.2. Furnace operation

The considered furnace (see Fig. 3) is a top-fired entrained flow gasifier, consisting mainly of a 2.5-m-long vertical tube, which makes up the primary reaction zone. The vertical walls of the furnace are electrically heated to a constant temperature of 1,300  $^\circ\text{C}$  to eliminate heat losses as an uncertainty during the experiments. This way, conditions in an industrial combustion reactor can be accurately replicated, and fuel properties can be evaluated. Excess air ratios (EAR, for definition, see Eq. 1) and oxygen enhancement levels were set and controlled using three separate mass flow controllers (MFC) for carrying-, primary- and secondary air. The burner features a circular central inlet, through which the PSS is fed, and three high-velocity nozzles with a rectangular shape to deliver the dominant momentum flux to the domain. An additional annular inlet is used to inject a secondary oxidizer to keep the flow

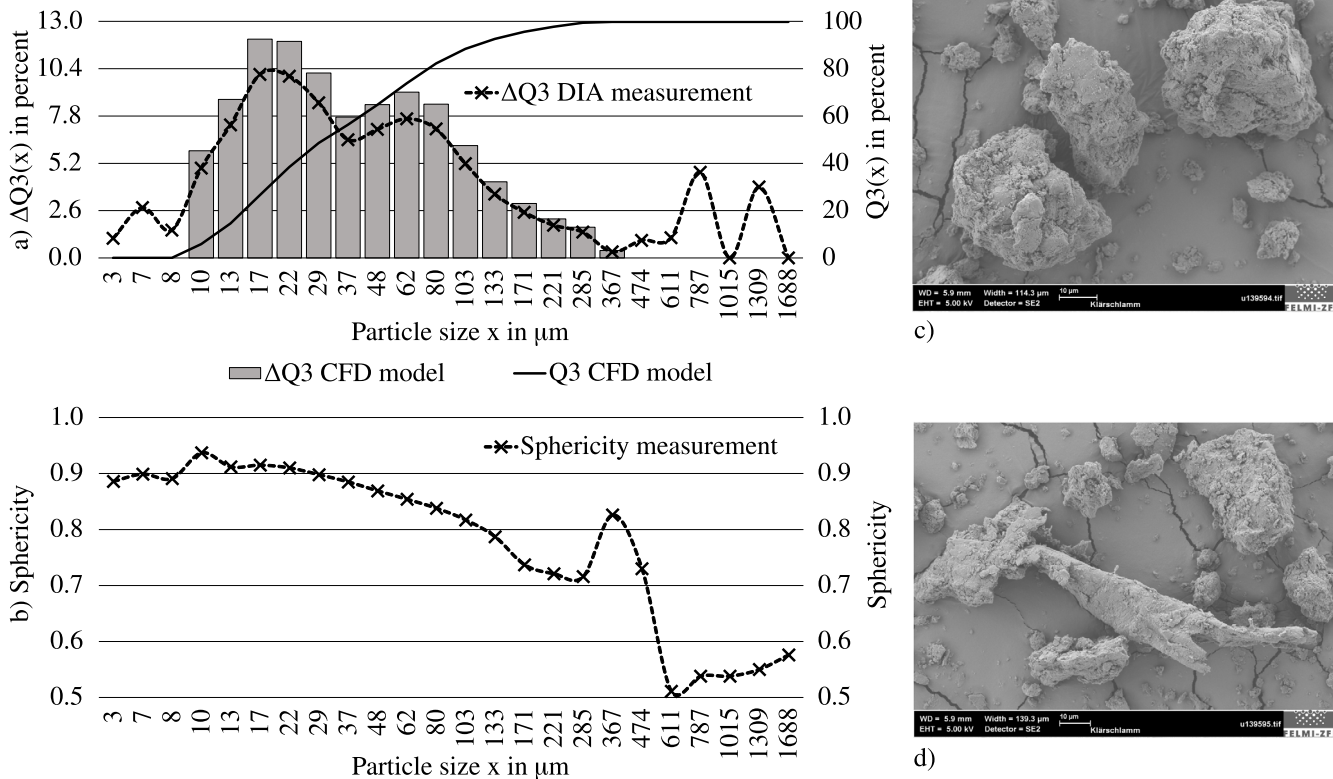


Fig. 1. (a) Particle size distribution - the grey columns represent classes, as defined in the CFD simulations, which mass-wise include fine and large particle fractions (b) Sphericity distribution, larger particles tend to be elongated. The vast majority exhibits sphericities around 0.85, which appear as shown in (c) under the SEM. An example of a non-spherical particle is given via the SEM image in d).

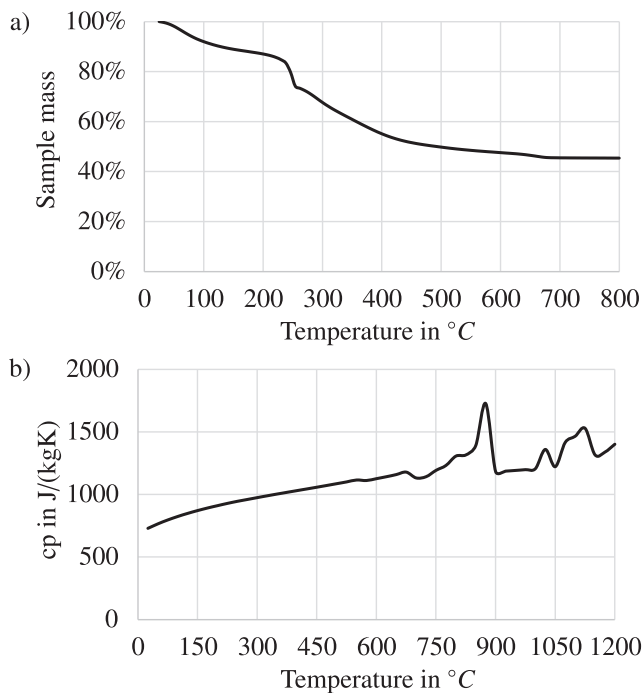


Fig. 2. Material properties (a) TGA curve at 10 K/min, (b) Specific heat capacity of the PSS particles.

conditions in different modes of operation comparable. Accurate powder dosage is achieved by a calibrated screw conveyor, which transports the fuel from a storage container towards a vibrating (to

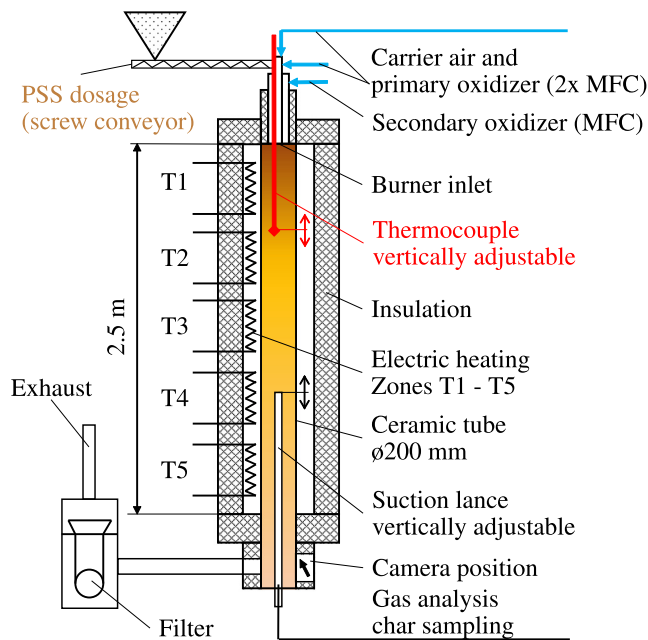


Fig. 3. Experimental reactor.

avoid clogging) dispersion zone. At this point, it is mixed with conveying air and injected into the reactor through a burner. The decline of mass in the storage container is monitored with a scale. The fuel mass flow was set to 3 kg/h. This low value was necessary to delay the slagging-related obstruction of the vertically adjusta-

ble suction lance used for flue gas measurements and particulate matter sampling.

$$\text{EAR} = \frac{\text{amount of oxidizer available}}{\text{stoich. required amount of oxidizer}} \quad (1)$$

The flue gas concentration was measured through the vertically adjustable suction lance, indicated in Fig. 3. From the fly-ash particle carrying flue gas stream, samples were taken and analyzed at different EAR and oxygen enhancement levels. All gas measurements were performed at a distance of 1.0 m from the burner inlet. CO, CO<sub>2</sub>, O<sub>2</sub>, H<sub>2</sub> and CH<sub>4</sub> measurements (dry-based) were taken at this distance to determine the flue gas composition. No changes were detectable further away than 1.0 m from the inlets. Due to the rapid accumulation of ash/slag, the openings of the suction lance would quickly become obstructed, making it difficult to take measurements closer to the burner. Fig. 4 shows the effect of slagging. The differences between Fig. 4a and 4c are caused by only a short operation time at low fuel mass flow rates of 3 kg/h. Closer than the aforementioned 1.0 m to the burner, measurements tended to become unstable and inaccurate.

A temperature profile measurement was possible using a vertically adjustable thermocouple inserted from the top through the burner, at a radial distance of 15.5 mm from the furnace axis. It can extend up to a maximum distance of 0.4 m from the inlet.

Within this study, we focus on two different modes of operation (Cases), which differ by the EAR and oxygen enhancement levels. These were chosen since they realistically represent plausible modes of operations of PSS conversion reactors.

- **Case 1:** Represents the over-stoichiometric combustion of PSS with air at an EAR = 1.2, which should guarantee complete burnout of the fuel.
- **Case 2:** Represents the sub-stoichiometric combustion of PSS at an EAR = 0.9 (slight gasification process), but with an oxygen-enhanced oxidizer (35vol% O<sub>2</sub>).

Because not enough oxygen is provided for complete combustion, the latter case produces a flue gas that can be used as a product gas, e.g., as a supplementary fuel in process engineering. With this gasification process, the heating value of the sewage sludge can be harnessed to a higher degree. The oxygen-enhancement is needed to reach similar temperatures as in the combustion process.

A main feature of this study is that the CFD results were compared with experimental data and observations. Such data points are difficult to obtain since sewage sludge as a fuel has specific undesirable properties, such as chemically aggressive slag and the tendency to form agglomerates.

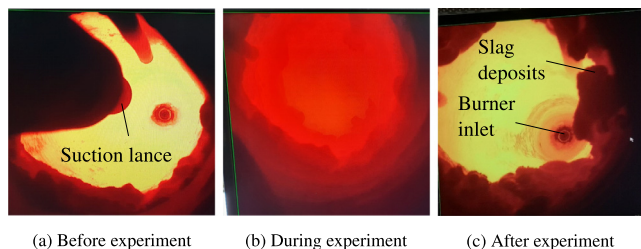


Fig. 4. View from the bottom of the reactor towards the burner inlet showing slagging due to the high ash content of the PSS. The direction of the view is indicated in Fig. 3 as "Camera position".

### 3. Numerical setup

This section explains the system's CFD modelling in detail, including basic information about turbulence, chemistry and radiation modelling and a description of the computational domain. All numerical calculations were performed using the commercial software code ANSYS Fluent 2020 R2.

#### 3.1. Multiphase flow

Since this study's main topic is applying a Flamelet-based model in both steady-state RANS and transient LES simulations, different approaches were taken to model the turbulent flow in the reaction chamber. For RANS, Favre-averaged Navier–Stokes equations are numerically solved using a pressure-based solver. Several turbulence models are tested, starting with the  $k-\omega$ -SST model from Menter et al. [34], which is often used and recommended, e.g., by Christ [35] or Chen [36]. It is suitable for furnace simulations since the implemented blending function allows the consideration of low-velocity regions in the primary reaction zone as well as the high velocities close to the burner inlets. As an additional eddy viscosity-based model, the realizable  $k-\epsilon$  model was applied, which is also commonly used in high-temperature process simulations such as in [37,38]. Furthermore, the most complex RANS model, the Reynolds stress modelling (RSM) approach is additionally used. It is more computationally demanding than the  $k-\omega$ -SST and the realizable  $k-\epsilon$  model, but less computationally expensive than transient LES simulations. These are the transient approach of choice within this study. In this method, larger eddies are resolved directly by the computational mesh, while smaller, energy-dissipating eddies have to be modelled using a subgrid-scale (SGS) model. The SGS stresses are considered using the wall-adapting local eddy-viscosity (WALE) model [39] within this study. The temperature-dependent density of the gas was considered using the incompressible ideal gas law. Since the simulation has to deal with a wide range of temperatures, the fluid's thermal conductivity and viscosity were also modelled temperature-dependent, using polynomial approaches.

In all simulations within this study, Lagrangian particle tracking via the discrete phase model (DPM) is implemented in a two-way coupled manner. The PSS particles emit combustible gases during their rapid devolatilization, determining the reaction zone. In steady-state simulations, the particulate mass flow enters the domain at the central pipe of the burner (see Fig. 5). A number of 22,000 representative particle streams (called "tries" in Fluent) is used to capture the stochastic behavior of the particle tracks in the system. Increasing the number of streams further did not alter the results. One particle track calculation was performed after every 15 fluid iterations. Stochastic tracking was implemented by means of the Discrete Random Walk (DRW) model with time scale constants of 0.15 ( $k-\omega$ -SST and realizable  $k-\epsilon$  model) and 0.3 (RSM) [40]. Because the PSD is poly-disperse, 15 discrete classes were implemented in CFD according to the grey bars in Fig. 1a. The non-spherical particle shapes were taken into account by considering class-wise shape factors according to Fig. 1b since larger particles exhibited lower sphericities in the DIA measurements. The sphericity is used as a shape parameter for the drag force calculations according to Haider et al. [41]. With this approach, particle shape information beyond standard correlations for spherical particles is included in the model. Due to the reasons outlined in the following section, mainly the small particle sizes, an even more detailed description of the particle shapes can be safely omitted, supporting the main focus of this study: a numerically inexpensive CFD model. The heat transfer to the particles results from thermal radiation and convective heat transfer. The latter was considered

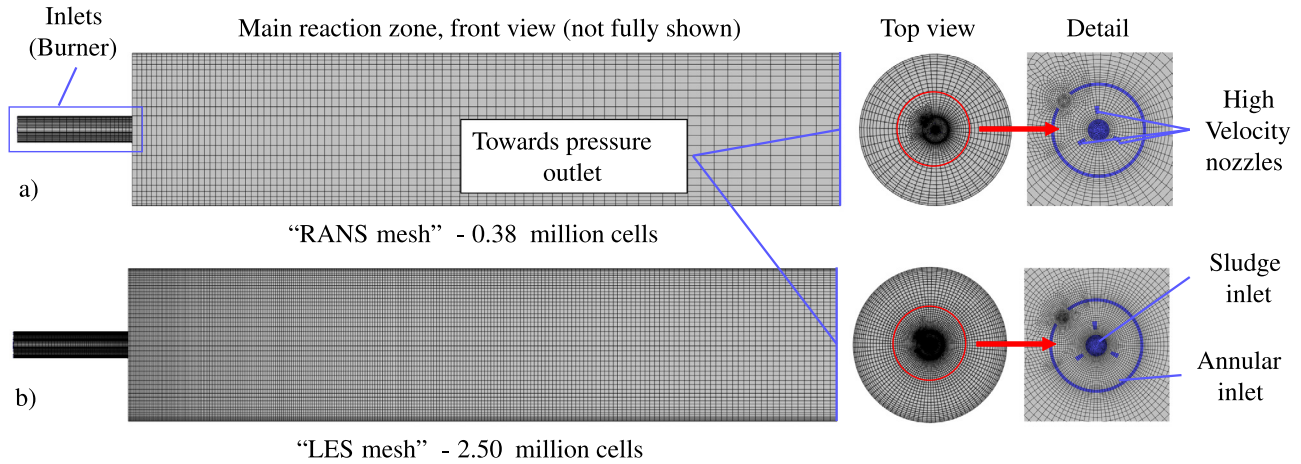


Fig. 5. Computational domains - (a) Coarse mesh, used for steady-state simulations and generation of initialization data (b) Fine mesh, used for final LES simulation.

by applying the correlation of Ranz et al. [42] according to the following energy balance Eq. 2 and the Nusslet number correlation in Eq. 3.

$$m_p c_p \frac{dT_p}{dt} = h A_p (T_\infty - T_p) + \varepsilon_p A_p \sigma (\Theta_R^4 - T_p^4) \quad (2)$$

$$Nu = \frac{hd_p}{\lambda_\infty} = 2.0 + 0.6 Re_p^{1/2} Pr^{1/3} \quad (3)$$

Therein,  $m_p$  stands for the particle mass, and  $c_p$  is the specific heat capacity of the particle according to Fig. 2b.  $T_p$  is the particle temperature, and  $A_p$  is its surface area. Furthermore,  $h$  is the heat transfer coefficient,  $\sigma$  is the Stefan-Boltzmann constant and  $Pr$  the Prandtl number ( $c_p \mu / \lambda_\infty$ ) of the continuous phase.  $\lambda_\infty$  is the thermal conductivity of the gas phase in the cell where the particle is located. Particle-radiation-interaction was considered for the calculation of heat transfer between the particles and the gas phase. In Eq. 2,  $\Theta_R = (\frac{G}{4\sigma})^{1/4}$  is the radiation temperature, where  $G = \int_{\Omega=4\pi} I d\Omega$  is the incident radiation and  $\Omega$  is the solid angle. A particle emissivity of  $\varepsilon_p = 0.9$  was used. Thermophoresis was not considered in the present study, since it is negligible compared to drag forces acting on the particles in the setup of our experiment. The near-wall region temperatures closely resemble those in the gas-phase due to wall heating. Consequently, only a negligible temperature gradient exists that could contribute to particle deposition associated with thermophoresis.

Due to the small particle size, the Biot number, defined according to Eq. 4, wherein  $V_p$  is the particle volume and  $\lambda_p$  its thermal conductivity (material property), is expected to be very low ( $Bi \ll 0.1$ ); therefore, intra-particle temperature gradients were omitted.

$$Bi = \frac{hV_p}{A_p \lambda_p} \quad (4)$$

The resulting Biot number will be evaluated in the result section of this study since it was implemented via an user-defined function (UDF).

The deposition criteria which is used to determine whether particles are sticking to the walls is based on that from Yong et al. [43]. They distinguished sticking and non-sticking particles and walls based on critical temperatures and Weber numbers. In our study, particles are considered to stick to the furnace walls after exceeding a critical temperature of 1,100 °C. The furnace walls are electrically heated to 1,300 °C and are therefore considered always sticky.

Since the particles enter the domain centrally and are only transported toward the walls by turbulent eddies, the expected Weber numbers are very low. Therefore, a Weber number-based distinction regarding slag deposition was not made within this study.

### 3.2. Computational domain

The computational domains applied in this study are shown in Fig. 5. Note that the domain's total length is not shown, but only up to a distance of 1.0 meters. Therefore, the pressure outlet at the bottom is not explicitly displayed. To ensure the validity of the assumptions underlying the DPM model, the discrete phase should not exceed a volume fraction of 10–12%. There are small cells within the thermocouples boundary, which are in the order of magnitude of the largest particle diameters (350  $\mu\text{m}$  for the finest mesh). In this case, a particle moving through the respective cell would locally violate the 12% limit. A particle with the median size of ca. 30  $\mu\text{m}$  however, would cause only a volume fraction of ca. 0.063 %. In the main flame zone, a particle volume fraction of 2e-3 (0.2 %) is hardly exceeded. Therefore, we are positive that the DPM model is a valid choice for our case.

Fig. 5a shows a coarse variant of the domain, featuring 389,260 mainly hexahedral cells. This mesh is the preferred choice for computationally inexpensive, steady-state RANS simulations. Fig. 5b shows the much finer resolved variant, called "LES mesh" which consists of 2,474,999 mainly hexahedral cells. A small number of wedge-type cells cannot be avoided due to the complex transitions from a circular main inlet (particulate matter and conveying air) in the center, a ring-like inlet for secondary air and three high-velocity nozzles in between. These deliver the majority of the momentum flux to the domain. Parts of the inlet ducts and nozzles upstream of the main reaction zone have been included in the mesh generation process. This was done to avoid the application of transient inflow conditions as they were not available for the setup at hand. A maximum skewness of 0.70 with an average value below 0.08 and a minimum orthogonal quality of 0.59 with an average value of 0.98 was achieved.

The meshes' suitability for the transient LES simulations was assessed according to Eq. 5, which characterizes the resolved proportion of the turbulence kinetic energy.

$$q = \frac{k_r}{k_r + k_m} \quad (5)$$

Therein, the resolved kinetic energy  $k_r$  is directly computed from the mean square velocity fluctuations. The modelled subgrid-scale

kinetic energy  $k_m$  is evaluated based on the subgrid-scale eddy viscosity  $\mu_t$ , density  $\rho$  and strain rate magnitude  $S$  [40].

$$k_r = \frac{1}{2}(\overline{u'w'} + \overline{v'w'} + \overline{w'w'}) \quad (6)$$

$$k_m = \frac{1}{0.3} \frac{\mu_t}{\rho} S \quad (7)$$

A  $q$  value of 0.8 or above indicates a sufficient resolution of the turbulent flow situation according to Pope [44], since 80 % of the turbulence kinetic energy is resolved. The evaluation offered in Fig. 6 indicates that the LES mesh can sufficiently meet this criterion. Only some minor zones inside the burner channels and directly at the PSS injection into the primary reaction zone exist, where values below 0.8 are observed. The resolution of the RANS mesh understandably shows poorer performance, with minimum values around 0.6, also in more relevant regions within the primary reaction zone. The general trends for both meshes are similar. The coarse RANS mesh was only used to obtain initialization data for the final LES case quickly. All other simulation results in this study are based on the finer mesh variant.

### 3.3. Combustion modelling

The SFM-based, non-premixed combustion model, a single-mixture-fraction approach, is briefly explained in this section. It enables the transient calculations, which are the main focus of this study. Multiple-mixture-fraction approaches for solid fuel combustion, are documented in the existing literature, such as in [21–23,25,29], and can describe the physics at hand in a greater level of detail. The adoption of a single-mixture-fraction approach in this study is a deliberate simplification, rooted in the specific material properties of PSS.

#### 3.3.1. Gas phase reactions

One requirement for the application of a non-premixed combustion approach to be accurate is that the most significant part of the chemical PSS conversion process is a matter of gas-phase reactions. The validity of this assumption has been pointed out in Section 1.1. Another requirement is the presence of turbulence in the flame zone, which is ensured by the momentum flux through the high-velocity nozzles of the burner. Due to their velocity of around 48 m/s, these guarantee a Reynolds number of at least 6,600 (case 2). What supports the application of a non-premixed-combustion approach further for our situation is the fine particle sizes and the high-temperature atmosphere in the experimental reactor. Moreover, TGA curves such as in Fig. 2a) are usually determined at moderate heating rates of 10–20 K/min, whereas the real heating rates in our reactor likely exceed  $10^5$  K/min. In essence, this forces the particles to devolatilize rapidly.

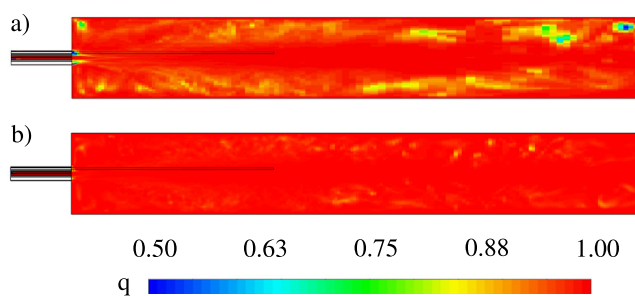


**Fig. 6.** LES resolution quality assessed via the proportion of the resolved turbulence kinetic energy. Based on 200 ms process time. (a) Coarse mesh, as used to obtain DPM initialization data (b) Fine mesh as used to obtain the final transient results.

In this study, the mass fractions of 0.409 (volatile matter), 0.100 (water content) and 0.041 (fixed carbon) in Table 2 are combined to one apparent devolatilization species, the surrogate fuel. This approach was considered justified under the assumption that the volatile fraction is high, the fixed carbon fraction is low, and the particles are thermally thin. Together with the assumption of equal diffusion rates for all elements, the combustion chemistry can be reduced to one transport equation for the mean mixture fraction  $\bar{f}$  and one for its variance  $\overline{f'^2}$ . The thermochemistry calculation can be performed and stored in look-up tables prior to the actual CFD simulation. The underlying chemical reaction mechanism for the chemistry tabulation is the *heptane42.che*-mechanism by Bui-Pham [45], which allows  $H_2$ ,  $H_2O$ ,  $CO$ ,  $CO_2$ ,  $N_2$ ,  $C_3H_6$  and  $C_7H_{16}$  as species for the surrogate fuel. This approach allows the inclusion of the effect which long-chain hydrocarbons may have on the combustion evolution. The composition of the surrogate fuel is determined by the original fuel's water content according to the proximate analysis, its H/C and O/C ratio, its stoichiometric oxygen demand and its lower heating value in MJ/kg. Since the resulting system of equations is complex, an *Excel* solver tool was used to minimize the deviations (H/C-, O/C-, LHV-error) by alternating the surrogate fuel compositions. The resulting composition is given in Table 3. Please refer to our previous publication [18] for details.

In contrast to conventional chemical equilibrium models, the SFM can consider slight non-equilibrium effects. The scalar dissipation at a stoichiometric condition  $\chi_{st}$  is the non-equilibrium parameter within the Flamelet framework. ( $\chi_{st} \rightarrow 0$  for chemical equilibrium). It is modelled as

$$\overline{\chi_{st}} = \frac{C_\chi \varepsilon \overline{f'^2}}{k} \quad (8)$$

in RANS simulations, whereas for LES simulations the mean scalar dissipation is modelled as in

$$\overline{\chi_{st}} = C_\chi \frac{(\mu_t + \mu)}{\rho \sigma_t} |\nabla \bar{f}|^2 \quad (9)$$

where  $C_\chi$  is a constant with 2 as the default value [40] and  $\sigma_t$  is the Prandtl number. An approach involving non-adiabatic energy handling was taken to create the PDF tables, which took into consideration radiative heat transfer resulting from non-adiabatic walls. In this context, it is assumed that any heat gain or loss would minimally impact the mass fractions of the species [46,47]. This is the currently available non-adiabatic energy treatment within *Ansys Fluent* [40]. Consequently, the temperature is computed across various mean enthalpy gain/loss levels, while species concentrations are taken from the adiabatic result. This is considered sufficient, since no significant low-temperature surfaces, which would contribute to a significant heat loss, are present in the furnace at hand.

#### 3.3.2. Devolatilization and char burnout modelling

The mass transfer between the particulate matter and the gas phase is considered using a single-kinetic rate approach. Therein, the devolatilization was modeled as linearly dependent on the amount of fuel remaining in the particle. The relevant parameters are the pre-exponential factor of  $A = 312,000 \text{ s}^{-1}$  and the activation energy of  $E_a = 7.4 \cdot 10^7 \text{ J/mol}$ . These values represent often-used values for lignite [40], which as pointed out above, has comparable volatile fractions to pulverized sewage sludge. Following the devolatilization process, the char burnout is modelled using a kinetics/diffusion limited approach with a rate constant of  $5 \cdot 10^{-12}$ , a pre-exponential factor of 6.7 and an activation energy of  $E_a = 1.138 \cdot 10^8 \text{ J/mol}$ . The char mass fraction is defined as 0.04 in the CFD model, so that volatile fraction, water content and char mass fraction combined equal to 0.55.

**Table 3**  
Surrogate fuel composition and flow boundary conditions.

Fuel Surrogate component	Mole fraction surrogate fuel 10% H <sub>2</sub> O(ar)	Flow specification	Case 1 in kg/h	Case 2 in kg/h
H <sub>2</sub> O	0.377	Sewage sludge (fuel)	3.000	3.000
H <sub>2</sub>	0.030	Feed air	2.714	0.900
CO	0.050	Annular pipe	5.400	1.350
CO <sub>2</sub>	0.300	High velocity nozzle	2.863	2.700
C <sub>3</sub> H <sub>6</sub>	0.030			
C <sub>7</sub> H <sub>16</sub>	0.121			
N <sub>2</sub>	0.090			

### 3.4. Radiation

The discrete ordinates model [48] together with a Weighted Sum of Gray Gases Model (WSGGM) [49] with standard coefficients from Smith et al. [50] was used to take into account the gas and black body radiation. An angular discretization of 3x3 was chosen for each octant. This model also allows to consider the necessary particle-radiation interaction, which further supports high heating rates. The particle-, wall- and thermocouple emissivity are assumed values. Nevertheless, the values are in a typical range for pulverized fuel combustion and slagging-related simulation studies. For instance, Akaotsu et al. used a particle emissivity of 0.85 for their simulation of pulverized coal combustion [29] while in this study, 0.9 was used for our PSS. From the visual appearance, PSS and coal powder are very similar. The same value was used for the walls due to slagging. This value was also applied in slagging related CFD models such as in the dissertation of Jønck [51]. An estimated value of 0.45 for the thermocouple emissivity was used for the simulation in this study. The thermocouple initially having a clean surface, will also be affected by slagging over time, to the point where it could not be removed from the furnace without destruction.

### 3.5. Boundary conditions

The mass flow boundary conditions were set according to Table 3, which shows all EAR and oxygen enhancement settings used in the simulations. An EAR below one relates to a fuel-rich process, whereas an EAR higher than one indicates fuel-lean (complete) combustion. The time step of  $2 \cdot 10^{-5}$  s in the LES simulations is the same for both cases, since the high-velocity nozzles determine the maximal time step size to maintain a Courant number below one. The inner reaction chamber walls with a diameter of 200 mm were set to keep a constant temperature of 1,300 °C, since they were electrically heated and controlled during the experiment. The thermocouple is modelled as a solid body as it is expected to have an influence on the flame. On the surface of the thermocouple, a no-slip boundary condition was applied. Sticky particles hitting the thermocouple surface are considered to be trapped.

### 3.6. Solution procedure and methods

To reduce the necessary simulation time, the solution of a steady-state simulation is obtained in three steps.

1. Solution of the oxidizer flow only, while considering the heated furnace walls until convergence is achieved (turbulent flow field, pressure-based coupled)
2. Inclusion of DPM particle tracking without considering the chemical reactions
3. Inclusion of the chemical reactions by activation of the transport equations for the mixture fraction and mixture fraction variance

Convergence was assessed according to residuals falling below  $10^{-6}$  for the energy, mixture fraction, mixture fraction variance and radiation and below  $10^{-3}$  for the continuity, momentum and turbulence equations. In addition to the residuals, monitoring temperatures, velocities and concentrations at various points in the domain over the iteration count was used to assess convergence. Pressure-velocity coupling was achieved using the SIMPLE (Semi Implicit Method for Pressure Linked Equations) algorithm when including the chemical reactions. PRESTO was used for pressure term discretization. Momentum, energy, turbulence and species-related transport equations were discretized using second-order upwind schemes. For radiation, a first-order upwind scheme was considered to be sufficient.

For the transient formulation, a bounded second-order implicit scheme was chosen. Generally, LES simulations should use a reasonably well-converged RANS solution for initialization [40]. This is done in this study, but with one significant amendment: When advancing from steady to transient, *Fluent* (at this point) cannot directly transfer the DPM-related particle track calculations results (e.g., positions, temperatures, volatile and char mass fraction etc.). Most notably, this causes the model to lose the particle-related source terms. Therefore, the steady-state flame result is immediately extinguished when starting the transient simulation. Ignition only restarts once particles, injected parcel-wise from the designated inlets, enter the reaction zone. This happens time step by time step, while the rest of the domain is suddenly void of particles. For the same reason, already burnt particles are also lost and cannot be considered for the calculation of particle-wall contacts and depositions. The implication is a loss of valuable computation time since a high number of time steps has to be calculated until statistical sampling can start. Realistically, two to three times the mean residence time has to be computed to reach a steady process state, which is not feasible at high cell counts and small time steps. This is especially true in cases where high-performance computing clusters are not accessible. Therefore, we implemented the following procedure:

1. Perform an LES simulation first on the coarse RANS mesh (see Fig. 5a) and compute three times the mean residence time  $t_{res,Case1}$ , which can be estimated using the domain volume  $V$  and the volumetric flow rate of flue gases  $\dot{V}$  with  $t_{res,Case1} = V/\dot{V} = 3.2$  s and  $t_{res,Case2} = V/\dot{V} = 6.0$  s. This can be done in around one to two days depending on the case, since a larger time step can be chosen and fewer iterations per time step are applied.
2. Write particle residence times, diameters, positions, velocities, temperatures, number in parcel and additionally the volatile and char mass fraction into an output file.
3. Create an injection file with additional columns for volatile and char mass fractions in *Matlab*.
4. Read the injection file at the very first time step of the simulation on the fine mesh. Additional lines for volatile and char mass fractions are read via UDF.

The numerous advantages of this approach are displayed in Fig. 7, which in a) shows the direct switch from RANS ( $k-\omega$ -SST model) to LES without initialization of the particles. The flame is blown out (1) and only starts to reignite after around 20 ms (2). Nevertheless, a cold spot remains (3), which prevents the early start of statistical sampling. Moreover, the loss of the source terms seems to create a reverse flow situation, which pushes the flame upwards together with buoyancy effects (4). In contrast, Fig. 7b shows that in the initialized case, particles instantly reignite (1). The steady-state result from the RANS solution gradually transforms into an instantaneous LES flame evolution (2), and no cold spots are observed. Also, the reverse flow problem does not appear.

On a hardware setup with a 16-core CPU and 64 GB RAM, a converged RANS solution (low residuals, steady monitors of physical quantities such as temperatures) on the coarse mesh can be achieved within only 3 h of computation time, including all particle track calculations. The fine mesh demands approximately 18 h to converge a steady-state simulation. Regarding the transient LES simulations: As mentioned previously, 1–2 days are necessary to generate the DPM initialization data on the coarse mesh. A final run on the fine LES mesh can be done in additional 3–5 days, depending on the desired quality of time-averaged results. Approximately one week is necessary to obtain the final time averaged LES results on the fine mesh.

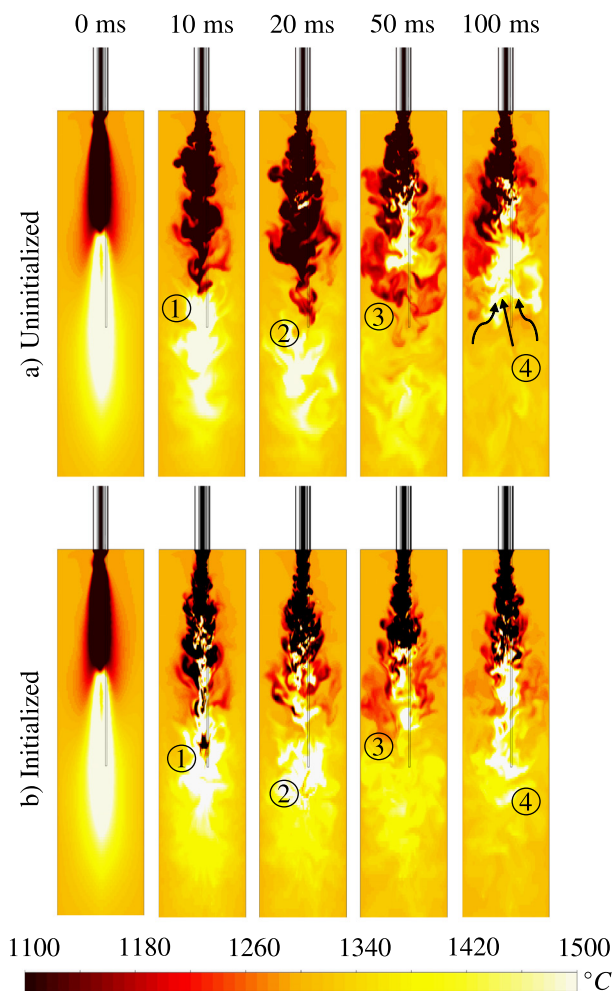


Fig. 7. a) Regarding DPM uninitialed case b) Regarding DPM initialized case 1 - Main differences: 1) Initialized particles ensure instant source term presence 2) Instant ignition of fresh fuel 3) Significantly reduced cold spots 4) Buoyancy-related reverse flow problem resolved.

## 4. Results and discussion

In this section, the major results are presented and discussed. Contour plots and data from temperature and species concentration measurements serve as a basis for evaluating the proposed CFD modelling approach. Direct measurements of particle wall contacts are hardly possible, and therefore, comparisons with the experiment are more of a qualitative nature, e.g., the experimentally determined quantitative value for particle-wall contacts (depositions) represents an average of case 1 and case 2 runs.

### 4.1. Species concentrations

It was not feasible to determine gas composition profiles experimentally due to heavy slagging during the experiment (closer to the burner), and therefore, the experimental results would have insufficient accuracy. Nevertheless, the main advantage of the SFM-based model compared to a standard chemical equilibrium (CEQ) approach will be discussed first using species concentration profiles. Experimental data at a distance of 1.0 m from the burner is available. Fig. 8 compares the main gas-phase results of the SFM-based model with CEQ model results (case 1). The graphic shows species concentrations (dry-based mole fractions) as axial profiles depending on the distance from the burner inlet. First, it should be noted that the results differ only very slightly. Still, they differ in some noteworthy details: The CEQ model results show significant peaks in the axial  $\text{CO}_2$  species profiles, which is not predicted by the SFM-based results. Furthermore, the CEQ model predicts much higher maximum CO concentrations than the SFM model. This confirms the SFM model's ability to consider slight non-equilibrium effects. It allows for the prediction of a more realistic combustion evolution. The increasing  $\text{O}_2$  concentration around 0.7 m from the burner inlet is caused by mixing effects in the furnace. The PSS particles are injected centrally whereas additional oxidizer enters the furnace at an extended radial distance. The figure shows that both modelling approaches agree on the location of the main reaction zones. The final results both agree very well with experimentally determined data. Because the experimental and simulation results match the equilibrium result at this EAR, it can be concluded that all particles burn out quite fully in this setup.

Often the ratio  $\text{CO}/\text{CO}_2$  is taken as a measure for the reducing conditions during a process and used in phase diagrams as in [52]. In this regard, the SFM-based model is more realistic since the gradual combustion evolution also allows for more realistic  $\text{CO}/\text{CO}_2$  values in the flame. Therefore, the proposed model can serve as a basis for in-depth particle kinetic modelling, which can be the subject of further studies.

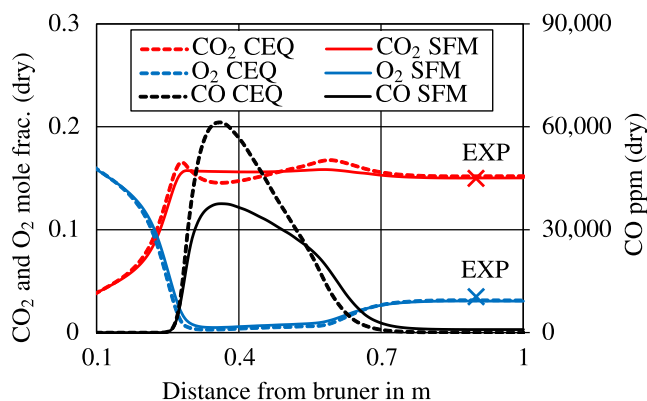


Fig. 8. Species concentration results for case 1, profiles through main furnace axis [18].

### 4.2. Particle conversion and temperatures

Fig. 9a shows the resulting temperature field for the SFM model simulation of case 1 considering an EAR of 1.2 and 21vol% O<sub>2</sub> in the oxidizer. From the top, cold oxidizer gas enters the domain in distinct jets, and some time is required to mix with the hot flue gases close to the burner inlet. The centrally injected particles heat up rapidly while mixing with the hot gases. The particle volatile mass fractions range up to 0.51, since the surrogate fuel also contains the water content as a part of the volatiles. Fig. 9b indicates that the process of devolatilization happens almost instantly. As soon as the particles mix with the hot gas phase, they lose their mass rapidly ("flash-devolatilization"). Therefore, the resulting flame is almost exclusively a result of gas-phase reactions. As pointed out above, this is due to the small size of the particles, the high heating rates and the high-temperature level in the drop tube furnace. Fig. 9c displays the particle Biot number, which does not exceed 0.04 even for the largest considered particles, which confirms the assumption of thermally thin particles. Note that for visibility purposes, the particle tracks are not displayed until termination but only for a limited number of particle time steps; otherwise, the entire visible domain would be filled with particles.

During the experiment, it was possible to measure temperatures in the furnace using the vertically adjustable thermocouple (see Fig. 3). For case 1, a comparison with the simulated values is given in Fig. 10. This graphic shows measured (crosses) and simulated (lines) temperatures in °C up to a distance of 0.4 m from the burner inlet. It can be argued that after an initial slight under-prediction of the temperatures, all models accurately predict the location of temperature increase and the final temperature levels. While all models agree on the final temperatures, the RANS-based models seem to underestimate the initial temperature increase close to the burner. The LES simulation is showing slightly superior results in this aspect.

The thermocouple measurement, which can be interpreted as a time-averaged value due to the thermal mass of the device, detects an excellent ignition behavior of the fuel directly after the injection. This is confirmed by the simulation result contours provided with Fig. 11. For the most part, all models agree on the flame location. The RSM and LES, however, predicted a slightly earlier ignition, as indicated by the horizontal line in the graphic. Furthermore, the  $k-\omega$ -SST variant predicts an elongated flame compared to all other models. While the  $k-\omega$ -SST and realizable- $k-\epsilon$  models have shown stable behavior, it should be noted that the RSM model predicted a slightly oscillating flame. In the

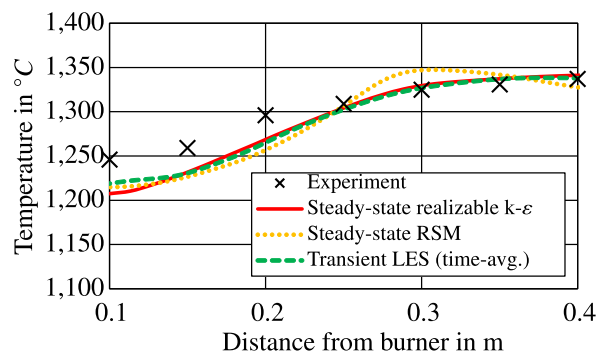


Fig. 10. Temperature profile for case 1 and comparison to SFM-based CFD results.

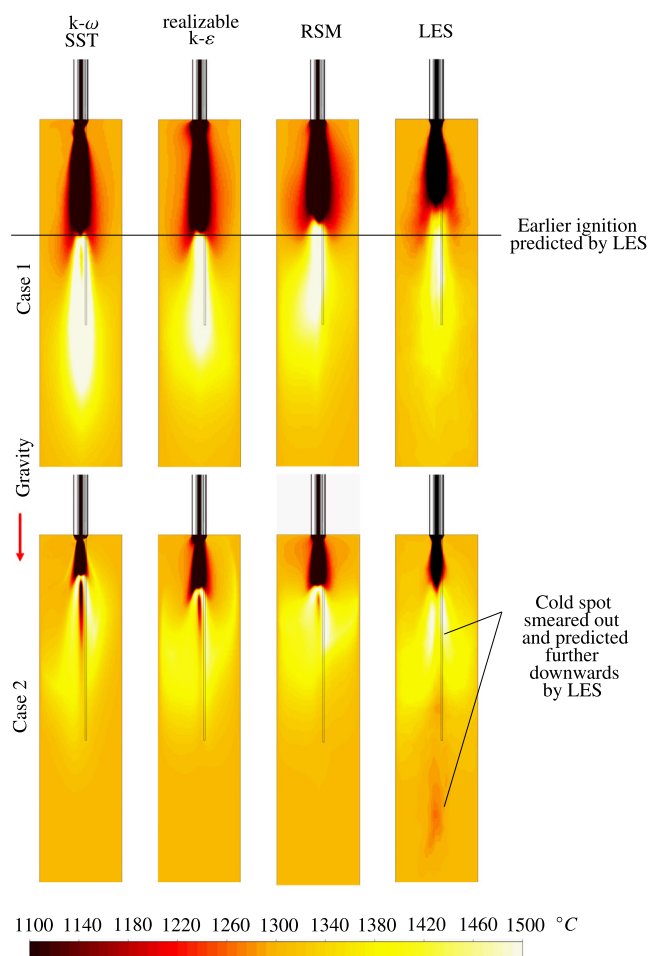


Fig. 11. Static temperature fields for case 1 and case 2, comparison of CFD results obtained with different models.

author's opinion, this effect is an indication of the (in reality) highly unsteady flame characteristics. The RANS simulation results of case 2 (bottom row in Fig. 11) agree with the LES result regarding the position of the flame. However, they all predicted a cold spot after the initial devolatilization of the particles started. This effect was most pronounced for the  $k-\omega$ -SST model and least noticeable in the RSM result.

After time-averaging the results of the LES simulation, the effect practically disappears. It becomes "smeared out" by the transient fluctuations of the temperature field. Instead, a cold spot, but less significant, was observed further down in the reaction zone. In any

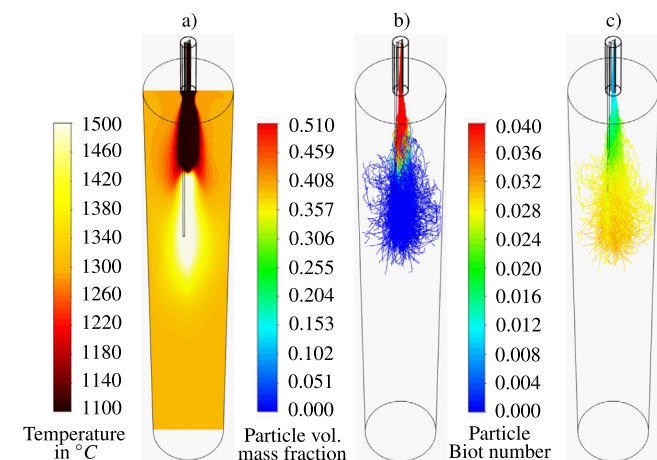


Fig. 9. Particle conversion - (a) Temperature field for case 1, (b) Particle volatile mass fraction, (c) Particle biot number as defined in Eq. 4.

case, this phenomenon is attributed to the ongoing heat-up of particles which already passed the devolatilization step (or are still in the process). The transient simulation seems to disperse the particle locations to a much higher degree, which explains the decrease in the initial cold spot location. The cold spot further down in the LES result is caused by large particles, which have higher mass and are subject to less dispersion. Their effect is more visible in the transient simulation results because the particle number per parcel was limited to values above one to ensure physically accurate results. This leads to large particles appearing less frequently and impacting time-averaged results to a higher degree. If multiple residence times were simulated in LES, which is computationally expensive, the effect would become more blurred. Overall the prediction accuracy improves with the complexity of the applied models, with LES showing the best performance but at the highest computational cost.

#### 4.2.1. Particulate matter balance

During the experiment, significant slagging was observed early after starting the trials. Fig. 4 gives an impression of the slag formation at the bottom of the reactor. After deposition, the slag slowly slid down through the 2.5 m long reactor tube, where it agglomerated further and eventually fell to the floor. Collecting and weighing the agglomerates was possible, which resulted in an approximate amount of 2.2 kg. This amount relates to an operating time of 5 h and 50 min, without interruptions for sampling and cleaning. Accounting for devolatilization and char burnout, this indicates that at least 28% of the occurring slag mass was deposited at the furnace walls. This amount must be considered a lower estimate because not all the slag might have fallen off in time, and a considerable fraction may still be in the furnace. It should be noted, that this value represents an average value for both cases. This is because it required a significant amount of time until the slag could be collected at the bottom. At this point, the collected matter could not be attributed to a specific case. The dominant momentum flux to the domain is delivered through the high-velocity nozzles, which were set to similar mass flow values for all cases to keep the flow conditions for the cases comparable.

During CFD simulations of case 1, it was noticed that all the RANS-based turbulence models significantly underestimated the amount of slag deposited at the furnace walls. The  $k-\omega$ -SST and RSM models yielded a trapped amount of 0.067 kg/h, while the realizable- $k-\epsilon$  model predicted 0.064 kg/h of particle deposition at the furnace walls. This amount relates to a percentage of around 5%, which is, beyond doubt, significantly below the experimental observations.

Upon initializing the LES simulation model using RANS data, our investigation focused on monitoring the trapped, escaped, and evaporated mass flow rates as they evolved over time. The corresponding profiles have been visually represented in Fig. 12. The findings reveal that following a simulation time of 0.1 s, all variables, particularly the rate of deposited particles, reach a constant level. However, inherent fluctuations are observed due to the unsteady nature of the flow. To determine LES deposition rates within the scope of this study, a statistical averaging approach was employed, specifically considering the LES simulation data from 0.1 to 1.0 s. Thereby, the transient LES simulations on the fine mesh increased the predicted amount of slag at the walls to 0.308 kg/h - which relates to 22.8%. The results are summarized in Fig. 13 for this case. In other words, LES simulations predicted roughly 4.6 times the slag accretion compared to the RANS models.

Through the utilization of the initialization approach, a significant threefold reduction in simulation time on the fine mesh was achieved, surpassing the need to compute multiple average residence times of around 3.2 s.

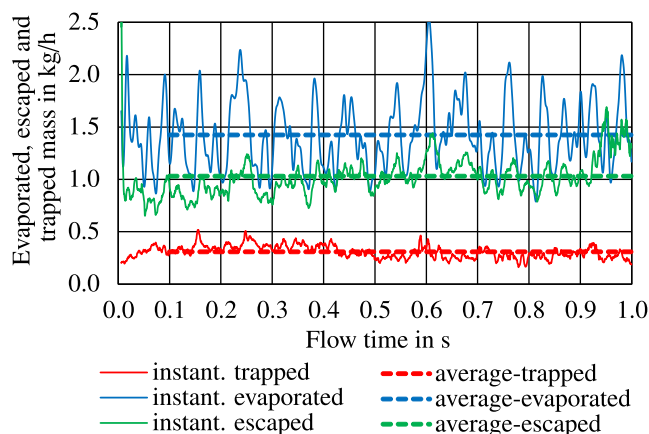


Fig. 12. Particle tracking results for case 1, obtained after initializing the transient LES simulation with RANS data.

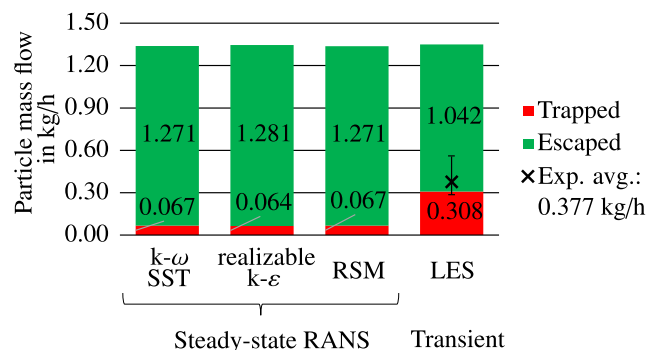


Fig. 13. DPM balance for combustion case 1.

Likewise, for the sub-stoichiometric case 2, RANS-based models agree well on roughly 0.090 kg/h of slag depositions at the furnace walls, which is a very similar value as in the combustion case 1. The LES model's deposition results are predicted significantly higher at 0.413 kg/h. The results are summarized in Fig. 14.

The sticking effect is visualized using Fig. 15, which shows contour plots of slag accretion at the furnace walls in  $g/(m^2s)$  ranging from blue (almost no particle-wall-depositions) to red (high occurrence of particle-wall-contacts). Compared to the temperature results, which appeared very similar for practically all models, the situation for slag accretion is entirely different. Overall, case 1 (top row) and case 2 (bottom row) show similar amounts of slag accretion. This similarity is attributed to the main momentum flux into the reaction zone provided by the three high-velocity nozzles.

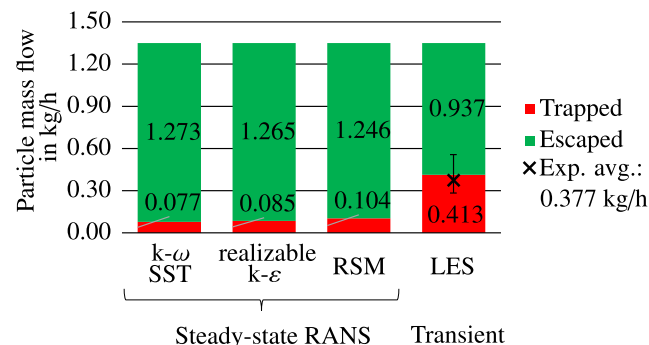


Fig. 14. DPM balance for sub-stoichiometric case 2.

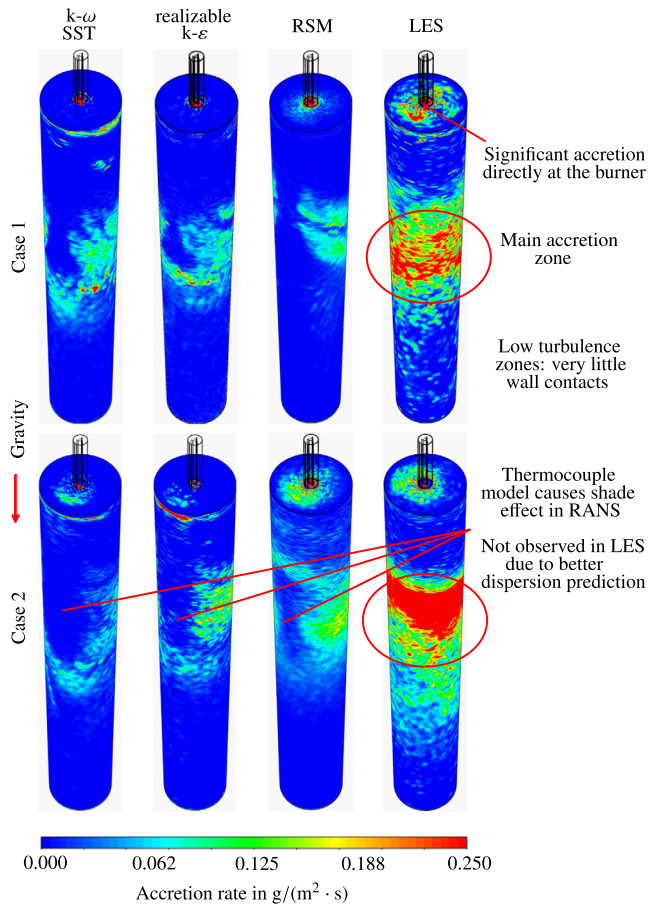


Fig. 15. Deposition rates in  $g/(m^2 \cdot s)$  for both cases.

Their velocity value is similar for both cases (see Table 3). There is, however, a striking difference between RANS and LES results. All RANS models predicted a meager amount of particle-wall contacts, contradicting the experimental observations. Additionally, a "shade" is visible in the RANS results, caused by the thermocouple's location within the geometry. The LES results show significantly higher accretion rates, and no influence of the TC is observed. This observation confirms a far more realistic prediction of the dispersion of particles by the LES approach. Additionally, much higher deposition rates are predicted at the top of the reaction chamber, which agrees very well with practical observations.

#### 4.2.2. Velocity fields and turbulence

The influence of turbulence modelling on temperature fields and particle depositions was presented in the previous sections. The following part will discuss the reason for the deviations between the results. In studies on slag formation in vertical furnaces such as that of Chen et al. [19], where slagging was modelled in significantly more detail, the basis was mostly a combustion simulation of a furnace that features a swirl-inducing burner. However, there is a significant difference between swirl burners and the burner used in our setup, especially regarding the average forces acting on particles inside the furnace. Since our burner only features vertical, to the furnace axis parallel channels for fuel and oxidizer injection, no distinct force field in radial direction will occur on a time-averaged basis. A swirl burner, on the other hand, will induce a swirling flow in the entire relevant domain and therefore generate constant centrifugal forces on the particles.

RANS simulations produce Favre-averaged results of all flow properties and are therefore incapable of taking into account the

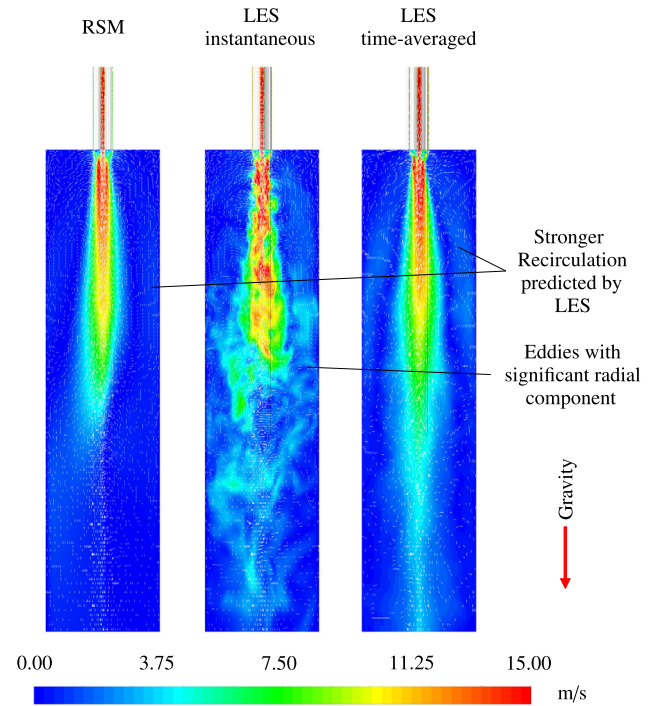


Fig. 16. Velocity fields.

instantaneous velocity fluctuations. These fluctuations (large-scale turbulent eddies) can have significant radial components and carry particles toward the furnace walls. LES is thus much more suitable for the prediction of particle-wall contacts, especially if non-swirling flames are considered. Fig. 16 compares velocity results of the best performing RANS simulation (RSM) with instantaneous and time-averaged large eddy results. The coloring reflects velocity magnitudes ranging from 0 to 15 m/s. Velocity vectors provide information about the flow directions and are uniformly sized.

The time-averaged and the instantaneous LES results display a significantly higher velocity upwards against gravity towards the burner inlet, where fresh fuel is injected. In the RANS simulations, this backflow is also present but to a lesser degree. Due to this backflow, hot flue gasses are redirected toward the burner. There they mix with fresh oxidizer and particle-laden carrying air, stabilizing the flame and promoting ignition. This effect is why the time-averaged LES results show a slightly higher flame position than RANS. Besides these effects, RSM results and time-averaged LES results of the velocity field appear very similar close to the burner. This supports the upstream-geometry including meshing approach instead of transient inflow conditions.

Particle-wall contacts and, therefore, slag depositions are predicted at elevated rates by LES. As seen in the instantaneous velocity contours, large eddies transport particles toward the walls, which does not happen in RANS simulations. This effect is so pronounced that more than four times the amount of slag depositions is predicted.

## 5. Conclusions and outlook

Steady-state RANS and transient LES simulations of sewage sludge combustion were performed and compared regarding chemistry and particulate matter balances. The application of a computationally inexpensive yet detailed chemistry-including approach facilitated LES simulations of the system. This strategy

allowed a comparison between steady-state and transient variants within a reasonable time.

It was shown that transient simulations massively improve the predictions of trapped particles at the walls of the investigated furnace with a non-swirl-inducing burner. Furthermore, the transient simulations predicted the local temperature distributions more accurately. They can additionally reveal more information about the time-dependent behavior of such systems while demanding acceptable computation times in industrial research and development and are therefore recommended.

Especially in systems with no significant swirl, properly initialized transient simulations can provide significantly more accurate predictions about the underlying process.

The suggested modelling approach additionally facilitates non-equilibrium gas-phase chemistry. It can therefore serve as a solid basis for the implementation of more detailed devolatilization models or even slag chemistry. The models provide solutions fast and can therefore be applied in the research and development of PSS burners and furnaces beyond academic research; in the industrial development and design of large-scale systems.

## Disclaimer

This publication reflects only the authors' views, and the European Health and Digital Executive Agency (HaDEA) and the European Commission are not responsible for any use that may be made of the information it contains.

## Declaration of Competing Interest

The authors declare that they have no known competing financial interests or personal relationships that could have appeared to influence the work reported in this paper.

## Acknowledgements

This project has received funding from the European Union's Horizon 2020 research and innovation programme under grant agreement No 958267.

## References

- W.D.C. Udayanga, A. Veksha, A. Giannis, G. Lisak, V.W.C. Chang, T.-T. Lim, Fate and distribution of heavy metals during thermal processing of sewage sludge, *Fuel* 226 (2018) 721–744.
- S. Aydin, A. Ulvi, F. Bedük, M.E. Aydin, Pharmaceutical residues in digested sewage sludge: Occurrence, seasonal variation and risk assessment for soil, *Sci. Total Environ.* 817 (2022) 152864.
- H. Namkung, Y.-J. Lee, J.-H. Park, G.-S. Song, J.W. Choi, Y.-C. Choi, S.-J. Park, J.-G. Kim, Blending effect of sewage sludge and woody biomass into coal on combustion and ash agglomeration behavior, *Fuel* 225 (2018) 266–276.
- M.M. Roy, A. Dutta, K. Corscadden, P. Havad, L. Dickie, Review of biosolids management options and co-incineration of a biosolid-derived fuel, *Waste management (New York, N.Y.)* 31 (11) (2011) 2228–2235.
- A. Bianchini, L. Bonfiglioli, M. Pellegrini, C. Sacconi, Sewage sludge management in Europe: a critical analysis of data quality, *Int. J. Environ. Waste Manage.* 18 (3) (2016) 226.
- L.M. Quan, H. Kamyab, A. Yuzir, V. Ashokkumar, S.E. Hosseini, B. Balasubramanian, I. Kirpichnikova, Review of the application of gasification and combustion technology and waste-to-energy technologies in sewage sludge treatment, *Fuel* 316 (2022) 123199.
- M. Atienza-Martínez, G. Gea, J. Arauzo, S.R.A. Kersten, and A.M.J. Kootstra. Phosphorus recovery from sewage sludge char ash. *Biomass and Bioenergy*, 65:42–50, 2014.
- Y. Wang, L. Yan, Cfd based combustion model for sewage sludge gasification in a fluidized bed, *Front. Chem. Eng. China* 3 (2) (2009) 138–145.
- S. Yani, X. Gao, H. Wu, Emission of inorganic pm 10 from the combustion of torrefied biomass under pulverized-fuel conditions, *Energy & Fuels* 29 (2) (2015) 800–807.
- C. Feng, J. Huang, C. Yang, C. Li, X. Luo, X. Gao, Y. Qiao, Smouldering combustion of sewage sludge: Volumetric scale-up, product characterization, and economic analysis, *Fuel* 305 (2021) 121485.
- J. Werther, T. Ogada, Sewage sludge combustion, *Prog. Energy Combust. Sci.* 25 (1999) 55–116.
- T. Ogada, J. Werther, Combustion characteristics of wet sludge in a fluidized bed, *Fuel* 5 (75) (1996).
- H. Cui, Y. Ninomiya, M. Masui, H. Mizukoshi, T. Sakano, C. Kanaoka, Fundamental behaviors in combustion of raw sewage sludge, *Energy & Fuels* 20 (1) (2006) 77–83.
- D.F. Fletcher, B.S. Haynes, F.C. Christo, S.D. Joseph, A cfd based combustion model of an entrained flow biomass gasifier, *Appl. Math. Model.* 24 (3) (2000) 165–182.
- H. Lin, X. Ma, Simulation of co-incineration of sewage sludge with municipal solid waste in a grate furnace incinerator, *Waste management (New York, N. Y.)* 32 (3) (2012) 561–567.
- A. Žnidarčič, T. Seljak, T. Katrašnik, Surrogate model for improved simulations of small-scale sludge incineration plants, *Fuel* 280 (2020) 118422.
- A. Žnidarčič, T. Katrašnik, I.G. Zsély, T. Nagy, T. Seljak, Sewage sludge combustion model with reduced chemical kinetics mechanisms, *Energy Convers. Manage.* 236 (2021) 114073.
- B. Ortner, C. Schmidberger, H. Gerhardtter, R. Prieler, H. Schröttner, C. Hoehenauer, Computationally inexpensive cfd approach for the combustion of sewage sludge powder, including the consideration of water content and limestone additive variations, *Energies* 16 (4) (2023) 1798.
- L. Chen, S.Z. Yong, A.F. Ghoniem, Modeling the slag behavior in three dimensional cfd simulation of a vertically-oriented oxy-coal combustor, *Fuel Process. Technol.* 112 (2013) 106–117.
- M. Knoll, H. Gerhardtter, C. Hoehenauer, P. Tomazic, Influences of turbulence modeling on particle-wall contacts in numerical simulations of industrial furnaces for thermal particle treatment, *Powder Technol.* 373 (2020) 497–509.
- J. Watanabe, K. Yamamoto, Flamelet model for pulverized coal combustion, *Proc. Combust. Inst.* 35 (2) (2015) 2315–2322.
- J. Watanabe, T. Okazaki, K. Yamamoto, K. Kuramashi, A. Baba, Large-eddy simulation of pulverized coal combustion using flamelet model, *Proc. Combust. Inst.* 36 (2) (2017) 2155–2163.
- X. Wen, K. Luo, Y. Luo, H.I. Kassem, H. Jin, J. Fan, Large eddy simulation of a semi-industrial scale coal furnace using non-adiabatic three-stream flamelet/progress variable model, *Appl. Energy* 183 (2016) 1086–1097.
- X. Wen, Y. Luo, K. Luo, H. Jin, J. Fan, Les of pulverized coal combustion with a multi-regime flamelet model, *Fuel* 188 (2017) 661–671.
- X. Wen, J. Fan, Flamelet modeling of laminar pulverized coal combustion with different particle sizes, *Adv. Powder Technol.* 30 (12) (2019) 2964–2979.
- M. Rieth, F. Proch, M. Rabaçal, B.M. Franchetti, F. Cavallo Marincola, A.M. Kempf, Flamelet les of a semi-industrial pulverized coal furnace, *Combust. Flame* 173 (2016) 39–56.
- M. Rieth, F. Proch, A.G. Clements, M. Rabaçal, A.M. Kempf, Highly resolved flamelet les of a semi-industrial scale coal furnace, *Proc. Combust. Inst.* 36 (3) (2017) 3371–3379.
- H. Watanabe, R. Kurose, Modeling and simulation of coal gasification on an entrained flow coal gasifier, *Adv. Powder Technol.* 31 (7) (2020) 2733–2741.
- S. Akaotsu, Y. Matsushita, H. Aoki, W. Malalasekera, Application of flamelet/progress-variable approach to the large eddy simulation of a turbulent jet flame of pulverized coals, *Adv. Powder Technol.* 31 (10) (2020) 4253–4274.
- A.H. Al-Abbas, J. Naser, D. Dodds, Cfd modelling of air-fired and oxy-fuel combustion in a large-scale furnace at loy yang a brown coal power station, *Fuel* 102 (2012) 646–665.
- M. Steibel, S. Halama, A. Geißler, H. Spliethoff, Gasification kinetics of a bituminous coal at elevated pressures: Entrained flow experiments and numerical simulations, *Fuel* 196 (2017) 210–216.
- H.A. Wadell, Volume, shape and roundness of rock particles, *J. Geol.* 40 (5) (1932) 443–541.
- L. Mu, S. Wang, Z. Zhai, Y. Shang, C. Zhao, L. Zhao, H. Yin, Unsteady cfd simulation on ash particle deposition and removal characteristics in tube banks: Focusing on particle diameter, flow velocity, and temperature, *J. Energy Inst.* 93 (4) (2020) 1481–1494.
- F.R. Menter, Zonal two equation k-w turbulence models for aerodynamic flows, *AIAA-93-2906* (1993).
- D. Christ. The effect of char kinetics on the combustion of pulverized coal under oxyfuel conditions: Zugl.: Aachen, Techn. Hochsch., Diss., 2013. Sierke, Göttingen, 1. Aufl. edition, 2013.
- L. Chen, A.F. Ghoniem, Simulation of oxy-coal combustion in a 100 kw th test facility using rans and les: A validation study, *Energy & Fuels* 26 (8) (2012) 4783–4798.
- R. Prieler, B. Mayr, M. Demuth, B. Holleis, C. Hoehenauer, Prediction of the heating characteristic of billets in a walking hearth type reheating furnace using cfd, *Int. J. Heat Mass Transf.* 92 (2016) 675–688.
- B. Mayr, R. Prieler, M. Demuth, C. Hoehenauer, Modelling of high temperature furnaces under air-fuel and oxygen enriched conditions, *Appl. Therm. Eng.* 136 (2018) 492–503.
- F. Nicoud, F. Ducros, Subgrid-scale stress modelling based on the square of the velocity gradient tensor, *Turb. Combust.* 62 (1999) 183–200.
- ANSYS Fluent Theory Guide, Release 2020 R2, ANSYS, Inc, Canonsburg, PA, USA.
- A. Haider, O. Levenspiel, Drag coefficient and terminal velocity of spherical and nonspherical particles, *Powder Technol.* 58 (1988) 63–70.
- W.E. Ranz, W.R.J. Marshall, Evaporation from drops, *Chem. Eng. Prog.* 48 (3) (1952) 141–146.

- [43] S.Z. Yong, M. Gazzino, A. Ghoniem, Modeling the slag layer in solid fuel gasification and combustion – formulation and sensitivity analysis, *Fuel* 92 (1) (2012) 162–170.
- [44] S.B. Pope. Ten questions concerning the large-eddy simulation of turbulent flows. *New J. Phys.*, 6(35), 2004.
- [45] M. Bui-Pham, K. Seshadri, Comparison between experimental measurements and numerical calculations of the structure of heptane-air diffusion flames, *Combust. Sci. Technol.* 74 (4) (1991) 293–310.
- [46] B. Binniger, M. Chan, G. Paczkko, M. Herrmann, Numerical simulation of turbulent partially premixed hydrogen flames with the flamelet model, *Combustion* (1998).
- [47] C.M. Muller, H. Breitbach, and N. Peters. Partially premixed turbulent flame propagation in jet flames. In 25th Symposium (Int) on Combustion, 1994.
- [48] G.D. Raithby, E.H. Chui, A finite-volume method for predicting a radiant heat transfer in enclosures with participating media, *J. Heat. Transf* 112 (1990) 415–423.
- [49] H.C. Hottel, A. Sarofim, *Radiative transfer*, McGraw-Hill Book Company, 1967.
- [50] T.F. Smith, F. Shen, N. Friedman, Evaluation of coefficients for the weighted sum of gray gases mode, *J. Heat Transfer* 104 (1982) 602–608.
- [51] K.M. Jønck. CFD Modelling of Melting Cyclones for Stone Wool Production, 2021.
- [52] K. Morita, N. Sano, 3 - phase diagrams, phase transformations, and the prediction of metal properties, in: *Woodhead Publishing Series in Metals and Surface Engineering*, 2005, pp. 82–108.